

# Intralayer Negative Poisson's Ratio in 2D Black Arsenic by Strain Engineering

Jingjing Zhang, Weihan Zhang, Leining Zhang, Guoshuai Du, Yunfei Yu, Qinglin Xia, Xu Wu, Yeliang Wang, Wei Ji, Jingsi Qiao,\* Feng Ding,\* and Yabin Chen\*

Negative Poisson's ratio as the anomalous characteristic generally exists in artificial architectures, such as re-entrant and honeycomb structures. The structures with negative Poisson's ratio have attracted intensive attention due to their unique auxetic effect and many promising applications in shear-resistant and energy absorption fields. However, experimental observation of negative Poisson's ratio in natural materials barely happens, although various 2D layered materials are predicted in theory. Herein, the anisotropic Raman response and the intrinsic intralayer negative Poisson's ratio of 2D natural black arsenic (b-As) via strain engineering strategy are reported. The results are evident by the detailed Raman spectrum of b-As under uniaxial strain together with density functional theory calculations. It is found that b-As is softer along the armchair than zigzag direction. The anisotropic mechanical features and van der Waals interactions play essential roles in strain-dependent Raman shifts and negative Poisson's ratio in the natural b-As along zigzag direction. This work may shed a light on the mechanical properties and potential applications of 2D puckered materials.

## 1. Introduction

Poisson's ratio  $\nu$ , as a fundamental mechanical property, is defined as the ratio of the induced transverse strain to axial strain.<sup>[1,2]</sup> For the isotropic materials,  $\nu$  can be principally expressed by  $\nu = [3(B/G - 2)]/[6(B/G + 2)]$ , where bulk modulus  $B$  and shear modulus  $G$  are associated with the volumetric and transverse deformations, respectively.<sup>[3]</sup> This relation essentially defines the numerical limits for Poisson's ratio,  $-1 \leq \nu \leq 1/2$  for  $0 \leq B/G < \infty$ , and most conventional materials generally have a positive Poisson's ratio. Negative Poisson's ratio (auxetic effect), an anomalous and interesting phenomenon, enables the lateral expansion instead of contraction when stretched lengthwise. With the prominent shear resistance, fracture toughness, and shock absorption, this specific kind of auxetic material possesses superior mechanical properties and is widely used in many practical fields, such as biomedical engineering, aerospace, sensor devices, and novel functional structures.<sup>[4-6]</sup> The negative Poisson's ratio effect

possesses superior mechanical properties and is widely used in many practical fields, such as biomedical engineering, aerospace, sensor devices, and novel functional structures.<sup>[4-6]</sup> The negative Poisson's ratio effect

J. Zhang, G. Du, Y. Yu, X. Wu, J. Qiao, Y. Chen  
Advanced Research Institute of Multidisciplinary Sciences  
Beijing Institute of Technology  
Beijing 100081, P. R. China  
E-mail: qiaoj@sbit.edu.cn; chyb0422@bit.edu.cn

J. Zhang, G. Du, Y. Yu, Y. Chen  
School of Aerospace Engineering  
Beijing Institute of Technology  
Beijing 100081, P. R. China


W. Zhang, W. Ji  
Beijing Key Laboratory of Optoelectronic Functional Materials  
& Micro-Nano Devices  
Department of Physics  
Renmin University of China  
Beijing 100872, P. R. China

L. Zhang  
Beijing Key Laboratory of Construction Tailorable Advanced Functional  
Materials and Green Applications  
MOE Key Laboratory of Cluster Science  
School of Chemistry and Chemical Engineering  
Beijing Institute of Technology  
Beijing 100081, P. R. China

Q. Xia  
School of Physics and Electronics  
Hunan Key Laboratory of Nanophotonics and Devices  
Central South University  
Changsha 410083, P. R. China

X. Wu, Y. Wang, J. Qiao  
MIT Key Laboratory for Low-Dimensional Quantum Structure and  
Devices  
School of Information and Electronics  
Beijing Institute of Technology  
Beijing 100081, P. R. China

F. Ding  
Faculty of Materials Science and Engineering/Institute of Technology for  
Carbon Neutrality  
Shenzhen Institute of Advanced Technology  
Chinese Academy of Sciences  
Shenzhen 518055, P. R. China  
E-mail: F.ding@siat.ac.cn

 The ORCID identification number(s) for the author(s) of this article can be found under <https://doi.org/10.1002/sstr.202300178>.

© 2023 The Authors. Small Structures published by Wiley-VCH GmbH. This is an open access article under the terms of the Creative Commons Attribution License, which permits use, distribution and reproduction in any medium, provided the original work is properly cited.

DOI: 10.1002/sstr.202300178

generally results from the special structure and deformation mechanism.<sup>[6–8]</sup> For decades, many efforts are extensively attracted to construct artificial structures with auxetic effect, including the re-entrant polymer foams ( $\nu = -0.7$ ),<sup>[9]</sup> honeycomb structures ( $\nu = -0.5$ ),<sup>[10,11]</sup> and carbon nanotube networks ( $\nu = -0.2$ ).<sup>[12]</sup>

It is with enormous challenge to explore a natural material with auxetic properties. Up to now, 2D layered materials have drawn considerable attention and exhibited many unique mechanical, optical, and electrical properties, including their super flexibility, thickness-dependent band structures, and quantum transport.<sup>[13–20]</sup> Their excellent mechanical properties of 2D materials allow us to demonstrate the strain engineering to modulate its lattice structure, carrier mobility, and electron–phonon coupling.<sup>[21–25]</sup> Importantly, it was found that many 2D materials, especially with puckered structures, can present negative Poisson's ratio, which can be categorized as two types: interlayer negative Poisson's ratio and intralayer negative Poisson's ratio.<sup>[26–31]</sup> For instance, group IV monochalcogenides (SiS, GeS, SnTe, etc.) are theoretically predicted to show cross-plane negative Poisson's ratio, that is, lattice constant  $z$  expands when stretching the structure along  $x$  direction.<sup>[32]</sup> Moreover, 2D elemental materials in group VA displayed the controversial Poisson's ratio properties. Raman spectrum and theoretical simulation by Du et al. demonstrated the auxetic effect of bulk black phosphorus (b-P) with both the obvious cross-plane interlayer and intralayer negative Poisson's ratio, through applying uniaxial strain along armchair (AC) direction.<sup>[26]</sup> In contrast, single-layer b-P with hinged structure even presented the cross-plane negative Poisson's ratio ( $\nu = -0.027$ ) when the uniaxial deformation along zigzag (ZZ) direction.<sup>[30]</sup>

2D black arsenic (b-As), as a cousin of b-P, has emerged recently and attracted extensive attention owing to its more stability and extremely anisotropic properties.<sup>[33,34]</sup> Its bandgap ranges from  $\approx 0.3$  (bulk) to  $\approx 1.4$  eV (monolayer),<sup>[35–37]</sup> and the carrier's mobility is as high as  $10^3 \text{ cm}^2 \text{ V}^{-1} \text{ s}^{-1}$  magnitude.<sup>[38,39]</sup> Compared with b-P, theoretical calculations showed that b-As exhibits a negative Poisson's ratio of  $-0.09$ , i.e., 3 times larger than that of b-P.<sup>[32,40,41]</sup> Moreover, it is predicted that b-As can withstand a larger strain limit. Accordingly, the mechanical properties of 2D b-As strongly depends on its lattice orientation and layer number.<sup>[42–44]</sup> It was found that the Poisson's ratio of few layer b-As becomes more negative and eventually approaches the limit ( $\nu = -0.12$ ) when the layer number goes to four.<sup>[29,32]</sup> Obviously, the internal mechanism remained elusive despite much effort, and the Poisson's ratio of b-As needs to be verified experimentally due to the lack of convincing experimental evidences.

In this work, we systematically investigated the uniaxial strain responses of three Raman vibration modes ( $A_g^1$ ,  $B_{2g}$ , and  $A_g^2$ ) of b-As based on two-point bending method combined with density functional theory (DFT) calculations. It was eventually revealed that intralayer negative Poisson's ratio characteristic exists in the natural b-As under strain along ZZ direction. Raman slopes of out-of-plane  $A_g^1$  mode and in-plane  $B_{2g}$  and  $A_g^2$  modes exhibit the distinct strain dependence when the uniaxial strain applied along in-plane AC and ZZ axes, respectively. The detailed DFT results confirmed that b-As is softer along AC than ZZ direction. In strain engineering, anisotropic mechanical features bring different variations of bond lengths and angles, leading to opposite Raman shifts. Our results can open up new avenues on the mechanical properties and future applications of 2D b-As.

## 2. Results and Discussion

It is well known that the artificial concave architecture can usually display negative Poisson's ratio property when its concave angle reaches a critical degree, as depicted in **Figure 1a**. Accordingly, as the tensile stress is applied along the horizontal direction, the inclined bars rotate and the concave angles increase remarkably, accompanied by the obvious expansion in the perpendicular direction.<sup>[6,45]</sup> Compared with this specific architecture, the natural b-As is predicted to feature negative Poisson's ratio property due to its in-plane anisotropic puckered structure in **Figure 1b**. In one atomic layer of b-As, each arsenic atom forms three  $\sigma$  bonds with  $sp^3$  hybridization, resulting in the in-plane covalent bonds longer than out-of-plane bond. This unique folded structure enables us to probe the extreme in-plane anisotropy, as reported in the orientation-dependent optical and electrical results.<sup>[36,40,46]</sup>

Two-point bending method<sup>[47–49]</sup> was used to apply the tunable and uniaxial strain along a given direction, where the b-As flake was located at the center of the flexible polyethylene terephthalate (PET, and its Young's modulus is as low as  $\approx 2.5$  GPa) substrate. **Figure 1c** represents a schematic diagram of our home-made setup, which is capable of in situ Raman characterizations under bending conditions. Meanwhile, this versatile setup can simultaneously realize the tensile and compressive states by flipping the entire device over. Strain is efficiently transferred to b-As sample through the flexible PET substrate. A thin polyvinyl alcohol (PVA) film was normally coated on the top surface of b-As and PET, in order to protect b-As from degradation in air and to prevent the interfacial slippage or corrugation of the sample during loading test as well. Based on the fundamental mechanics, the applied strain ( $\epsilon$ ) can be expressed as  $\epsilon = \tau(\sin\theta)/2a$ , where  $\tau$  denotes the PET thickness,  $\theta$  represents the angle between the tangent and horizontal directions at the endpoints of the flexible substrate, and  $2a$  is the distance between two loading endpoints.<sup>[3,50]</sup> The detailed derivation is given in **Figure S1**, Supporting Information.

Raman spectrum of 2D layered material, as a powerful means to probe the structural change and electron–phonon coupling, is quite sensitive to the external force field. **Figure 1b** displays three typical phonon vibration modes of b-As crystal, including the out-of-plane  $A_g^1$  and the in-plane  $B_{2g}$  and  $A_g^2$ . It is obvious that the dominant components of  $B_{2g}$  and  $A_g^2$  modes vibrate along the ZZ and AC directions, respectively. Crucially, the  $A_g^1$  mode, describing the relative motions of arsenic atoms at the top and bottom, can rationally reveal the possible out-of-plane negative Poisson's ratio of the puckered b-As.

To evaluate the lattice orientation and crystal quality of b-As specimen, angle-resolved polarized Raman measurements and high-resolution transmission electron microscopy (HRTEM) were performed on various b-As flakes (**Figure S2**, Supporting Information). First of all, large-area b-As flakes were mechanically exfoliation onto PET surface using scotch tape (see the Experimental Section for more details). The thickness of b-As flakes was examined by its optical contrast and also precisely determined by atomic force microscopy (AFM). Afterward, polarized Raman spectroscopy was attempted to distinguish the AC and ZZ directions of b-As. As far as we know, Raman intensity of  $A_g$  modes of b-As is profoundly affected by the sample thickness and excitation wavelength because of the anisotropic

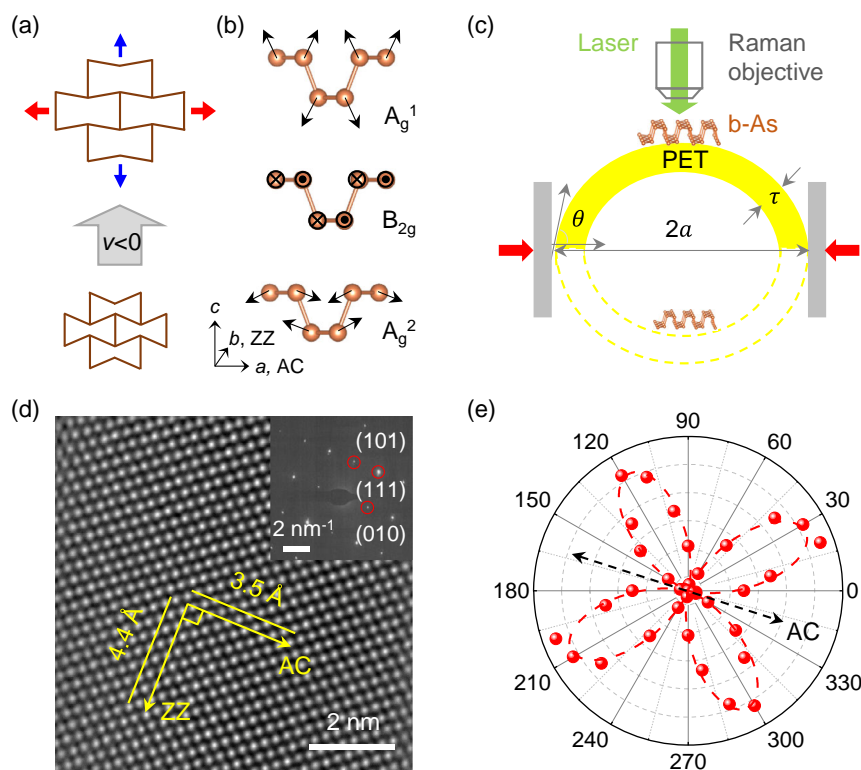


**Figure 1.** Strain engineering in b-As and its structural characterizations. a) The typical concave architecture that basically shows a negative Poisson's ratio. The structure expands perpendicularly when the tensile strain applied along horizontal direction. b) Schematic diagram of crystal structure of b-As and three typical Raman modes. It is noted that  $A_g^1$ ,  $B_{2g}$ , and  $A_g^2$  vibrate along out-of-plane, in-plane ZZ, and AC directions, respectively. c) Schematic diagram of our home-made bending setup. The uniaxial strain can be tuned by bending a flexible PET substrate with a b-As flake on the top. This setup enables to apply compressive strain as well (dashed lines). d) HRTEM image of b-As with atomic resolution. The ZZ and AC directions are marked clearly. Inset is the SAED pattern. e) Polarized Raman diagram of  $B_{2g}$  mode as a function of the angle  $\theta$  between laser polarization and AC direction. The red dashed line shows the fitting result with  $I \propto \sin^2(2\theta)$ . The black arrow indicates the AC direction.

interference and absorption effects.<sup>[51]</sup> In contrast, Raman intensity of  $B_{2g}$  mode remains unchanged and shows the repeated polarization dependence.<sup>[36,52]</sup> As shown in Figure 1e, in the parallel configuration, when the two main lattice axes are aligned with the laser polarization, the  $B_{2g}$  mode cannot be detected due to matrix cancellation. Therefore, it allows us to conveniently identify the ZZ or AC directions of b-As flake. In addition, the results were completely confirmed by HRTEM image and selected-area electron diffraction pattern. In Figure 1d, the orthorhombic structure is distinct and further evidenced by the lattice spacing of 4.5 and 3.7 Å along the AC and ZZ directions, respectively, well consistent with our theoretical results ( $a = 4.46$  Å,  $b = 3.74$  Å, and  $c = 11.03$  Å).

Next, strain-dependent Raman shifts, theoretical calculations, and the systematic analysis of b-As flake were demonstrated to explore the uniaxial strain-induced structural transformation and Poisson's ratio along the different AC and ZZ orientations, respectively. For the natural b-As without any deliberate strain, Raman shifts of  $A_g^1$ ,  $B_{2g}$  and  $A_g^2$  modes are fitted as 219.82, 225.87, and 253.58  $\text{cm}^{-1}$  in the parallel-polarized configuration, respectively. **Figure 2a** shows the detailed evolution of the acquired Raman spectra of b-As under uniaxial strain along AC direction. The applied strain ranged from the tensile

+0.31% to compressive -0.31%. It is noted that both  $B_{2g}$  and  $A_g^2$  modes show a slight blueshift as the strain gradually increases; however,  $A_g^1$  mode inversely exhibits an obvious redshift. As illustrated in Figure 2b, the linear rates of  $A_g^1$  mode are extracted as  $-2.13$  and  $-1.86 \text{ cm}^{-1} \%$  under the compressive and tensile strain, respectively. In comparison,  $A_g^2$  mode hardened as increasing strain, and the corresponding rates are 0.58 (compression) and 0.50 (tension)  $\text{cm}^{-1} \%$ . For a specific phonon mode, the rate difference between compressive and tensile strains is primarily attributed to the nonmonotonic response on the interlayer and intralayer couplings. The data points of  $B_{2g}$  mode seem fairly scattered, accompanied with a negligible shift rate, which basically results from this special vibration mainly along ZZ direction, and hence it is insensitive to the external stimulus along AC direction.

When the strain was loaded along ZZ direction, Figure 2c,d displays the significantly different results from the former. Apparently, both the in-plane  $B_{2g}$  and  $A_g^2$  vibration modes experience clear redshift when the tensile strain is stretched along ZZ direction, with a slope of  $-6.00$  and  $-2.67 \text{ cm}^{-1} \%$ , respectively. On the other hand,  $B_{2g}$  and  $A_g^2$  modes have a blueshift at a rate of  $-5.48$  and  $-2.61 \text{ cm}^{-1} \%$  as the compressive strain, as shown in Figure 2d. Although these two models exhibit the

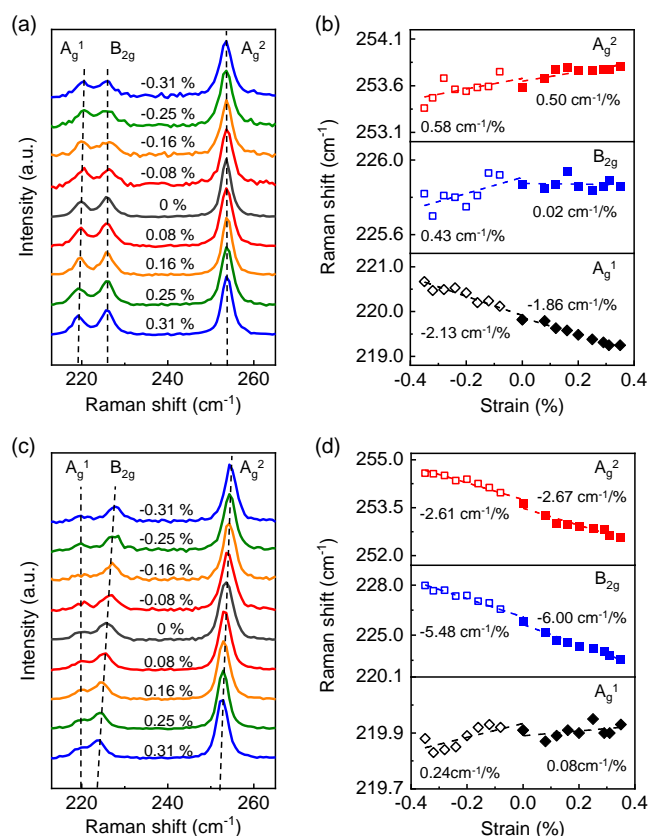


**Figure 2.** Raman spectra of b-As (15.8 nm thick) under uniaxial strain along different directions. a) Raman spectrum evolution of b-As when the strain applied along AC direction. b) Raman shifts of  $A_g^1$ ,  $B_{2g}$ , and  $A_g^2$  modes as a function of strain along AC direction. c) Strain-dependent of Raman spectrum of b-As with strain along ZZ direction. d) Raman shifts of three phonon modes as a function of strain along ZZ direction. Dashed lines show the linear fitting results.

same trends, the slope of  $B_{2g}$  mode is about twice larger than that of  $A_g^2$  mode. It can be attributed to the fact that  $A_g^2$  mode vibrates along in-plane AC direction, so it is insensitive to the strain in ZZ direction. Meanwhile, the out-of-plane  $A_g^1$  mode presents a faint blueshift due to the relatively scattered data, which arises from its intrinsically weak Raman intensity in ZZ direction.

To understand the Raman results and further explore its internal mechanism, we first performed DFT calculations with the optB86b to investigate the geometric and vibrational properties of strained b-As (see DFT methods for more details).<sup>[53,54]</sup> We labeled the lattice parameters highly related to vibrational modes in Figure 3a,b, including three lengths ( $R_1 \approx R_3$ ), the projection distances of  $R_2$  ( $R_{2x}$ ,  $R_{2z}$ ), and two bond angles  $\theta_1$  and  $\theta_2$ . Based on the atomic displacements of three phonon modes in Figure 1b, their strain dependence of Raman shifts can be analyzed in depth according to the relative lattice deformation. In detail,  $A_g^1$  mode reflects the cross-plane vibration of arsenic atoms as discussed above, which is mainly sensitive to intralayer bond length  $R_2$  and bond angle  $\theta_2$ . As shown in Figure 3c,e, when the strain was applied along AC direction, the lattice constants of  $a$  and  $c$  shorten apparently, while bond length  $R_2$

elongates, leading to the weakened interatomic interaction and the reduced Raman frequency of  $A_g^1$ . Instead, both in-plane  $B_{2g}$  and  $A_g^2$  vibrations are related to bond length  $R_1$  and bond angle  $\theta_1$ . The blueshifts of  $A_g^2$  and  $B_{2g}$  modes are attributed to their enhanced As–As interactions due to the decreased in-plane bond lengths  $R_1$  and bond angle  $\theta_1$ . Interestingly, the Raman shift trend along ZZ direction is completely opposite to that along AC direction, which results from their unique response of lattice structure to the external strain in Figure 3f–h. In this case, bond length  $R_1$  elongates and both  $R_2$  and  $R_3$  shorten, along with the reduced  $\theta_2$  and larger  $\theta_1$ . In general, b-As is softer along AC than ZZ direction. Anisotropic mechanical features result in different responses of bond lengths and angles, inducing the distinct strain-dependent Raman shifts uniaxial strain engineering.

Furthermore, we comprehensively discuss the fascinating Poisson's ratio properties of b-As by DFT calculations with different functionals, including Perdew–Burke–Ernzerhof (PBE, without van der Waals [vdW] correction),<sup>[55]</sup> optB86b-vdW, and DFT-D3.<sup>[56,57]</sup> It is well known that vdW interaction plays a vital role in physical properties of 2D layered systems, especially for Group V elemental nanomaterials.<sup>[58]</sup> After optimizing the lattice structure using optB86b-vdW functional, we found that lattice constant  $c$  was synergistically determined by out-of-plane projection  $R_{2z}$  and interlayer distance  $R_3$ . The results of optB86b-vdW method showed that the interlayer distance  $R_3$  remains almost constant, while both  $R_{2z}$  and lattice constant  $c$  decrease slightly under the strain along AC direction, indicating that there is no omitted negative Poisson's ratio effect in sublayers or interlayer. These results were further verified by DFT-D3 functional in Figure S6, Supporting Information, distinguished from PBE functional without considering vdW correction. The PBE functional displayed that both  $R_3$  and lattice constant  $c$  increased when the strain along AC direction, suggesting an obvious interlayer negative Poisson's ratio in Figure S7, Supporting Information. This phenomenon is controversial, although it is inclined to agree with the literature result of b-P.<sup>[26]</sup> Notably, Figure 3g illustrates that out-of-plane projection distance  $R_{2z}$  increases significantly as the tensile strain applied in ZZ direction, consistent with the theoretical results of monolayer b-As,<sup>[29]</sup> so it is confirmed that the natural b-As has intralayer negative Poisson's ratio in this scenario. Importantly, this unique property should be remained as the thickness of black arsenic approaches the monolayer limit.

Subsequently, thickness-dependent Raman shift rates in  $A_g^1$ ,  $B_{2g}$ , and  $A_g^2$  modes of b-As were further investigated under the same strain condition. After the bending test, the PVA film was removed by DI water and the sample thickness was accurately measured by AFM technique, as shown in Figure S2, Supporting Information. In Figure 4, it can be seen that all  $A_g^1$ ,  $B_{2g}$ , and  $A_g^2$  modes clearly present the similar anisotropic trends along different directions. When the tensile or compressive strain was along ZZ direction, the Raman slopes of in-plane  $B_{2g}$  and  $A_g^2$  modes decrease obviously as the flake thickness increases. Raman slope  $K$  is defined as  $K = \partial\omega/\partial\varepsilon$ , where  $\omega$  and  $\varepsilon$  are the Raman shift and the applied strain, respectively. It can be explained that mechanical properties of thinner b-As are less affected by the interlayer coupling. However, the results

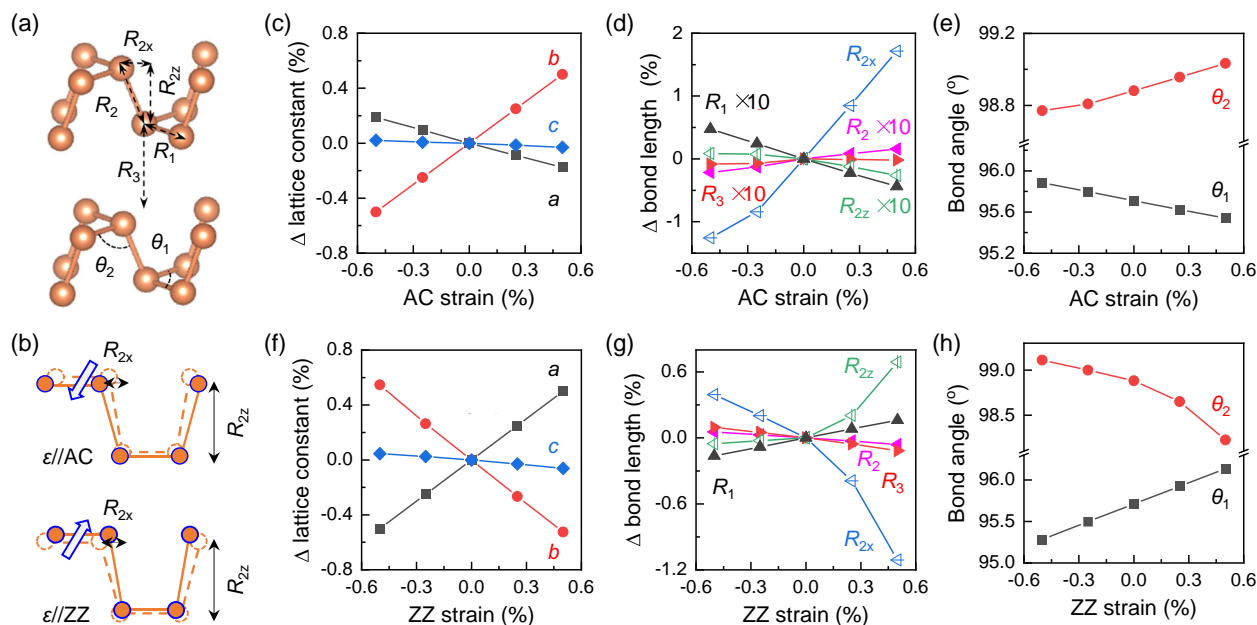


**Figure 3.** Intralayer negative Poisson's ratio and the microscopic mechanics in 2D b-As when the strain was applied along ZZ direction. a) Atomic structure of b-As flake with the labeled bond lengths and angles. b) Schematic illustration of lattice deformations of b-As under uniaxial strain along AC (top) and ZZ (bottom) directions. c) Lattice constants  $l$  evolution of b-As as strain along AC direction.  $l\% = (l_s - l_0)/l_0$ , where  $l_s$  and  $l_0$  denote the lattice constant with and without strain for  $a$ ,  $b$ , and  $c$ , respectively. d) The normalized bond lengths vary as the strain along AC direction.  $R\% = (R_s - R_0)/R_0$ , where  $R_s$  and  $R_0$  represent the bond length with and without strain, respectively. e) Strain-dependent bond angles of b-As along AC direction. f) Lattice constants evolution of b-As as strain along ZZ direction. g) The normalized bond lengths vary as the strain along ZZ direction. h) Strain-dependent bond angles of b-As along ZZ direction.

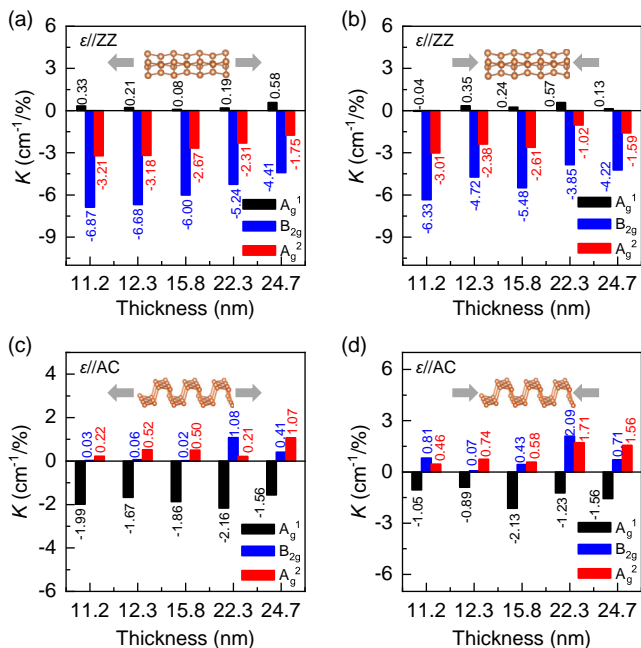


**Figure 4.** Thickness-dependent Raman responses of b-As sample under uniaxial strain. a) Thickness dependence of Raman shift rates ( $K = \partial\omega/\partial\varepsilon$ ) of three modes under tensile strain along ZZ direction. b) Thickness dependence of Raman shift rates under compressive strain along ZZ direction. c) Thickness dependence of Raman shift rates of three modes under tensile strain along AC direction. d) Thickness dependence of Raman shift rates under compressive strain along AC direction.

along AC direction present little difference with the flake thickness, and the fluctuation of experimental data is significant.

### 3. Conclusions

In summary, we have demonstrated the intralayer negative Poisson's ratio property in the natural 2D b-As with puckered structure, evidenced by the uniaxial stress-regulated Raman spectrum and the detailed DFT calculations. The strain engineering based on two-point bending method proved the anisotropic response of  $A_g^1$ ,  $B_{2g}$ , and  $A_g^2$  phonon modes when strain applied along AC and ZZ directions, well consistent with our theoretical results. Intralayer negative Poisson's ratio of b-As was confirmed with the anomalous Raman response to both compressive and tensile strain along ZZ direction. DFT calculations clarified that anisotropic mechanical features induced different responses of bond lengths and angle, and further vdW interaction played the critical role in Poisson's ratio characteristic. We believe these results could boost the research on mechanical properties of anisotropic 2D materials and further promote their wide applications.

### 4. Experimental Section

**Preparation and Characterization of b-As Flake:** The b-As sample used in this work was cleaved from the natural mineral. Then, the b-As flake with different thickness was mechanically exfoliated to a flexible PET substrate using Scotch tape. The PET substrate was shaped to square (the

dimension of 25 mm × 25 mm, and about 230 μm thick) and the b-As was located at the center of PET surface, which are convenient to the alter strain engineering process. Combined with the transmission and reflection observations of optical microscope, b-As thickness can be roughly estimated. AFM was used to accurately determine its thickness after the bending test. Importantly, a PVA coating was essential to prevent oxidation and slippage of b-As flakes, and the PVA layer can be easily washed away with DI water.

**Raman Spectrum Measurements:** All Raman measurements were performed on the Horiba iHR550 system. 633 nm laser was used to excite the angle-resolved polarized Raman spectrum. For polarized Raman measurements, the analyzer was set parallel to the incident polarization direction of the laser. Then the angle-resolved polarization Raman spectrum was acquired by rotating the sample from 0° to 180°. Raman spectrum under uniaxial strain was measured using 532 nm laser. All characterizations were performed with a100× objective lens and a grating of 1800 grooves mm<sup>-1</sup>. The laser beam was focused as about 1 μm and spectral resolution was better than 0.1 cm<sup>-1</sup>. The weak laser power as ≈20 μW was used to protect the b-As sample from the potential heating effect.

**DFT Calculations:** DFT calculations were performed using the generalized gradient approximation for the exchange–correlation potential, the projector augmented wave method, and a plane-wave basis set as implemented in the Vienna ab initio simulation package.<sup>[59–61]</sup> Density functional perturbation theory was employed to calculate vibrational frequencies at the G point.<sup>[62]</sup> The vdW density functional method was used to describe the vdW interactions together with the optB86b exchange function,<sup>[54,63]</sup> which is proved to be accurate in reproducing atomic structure of layered materials.<sup>[64]</sup> The energy cutoff for the plane-wave basis was set to 700 eV for all calculations. A k-mesh of 31 × 31 × 15 was adopted to sample the first Brillouin zone of the conventional unit cell of bulk b-As in geometric optimization and phonon frequencies. The shape of each cell was optimized fully and all atoms in the cell were allowed to relax until the residual force per atom was less than 1 × 10<sup>-4</sup> eV Å<sup>-1</sup>. For PBE and DFT-D3 functionals, the calculations were performed with the projector augmented wave method.<sup>[61]</sup> The exchange–correlation functions were treated by the PBE generalized gradient approximation.<sup>[55]</sup> Despite the PBE functional described the chemical bonding between arsenic atoms well, it normally ignores the dispersion interaction. In addition, the DFT-D3 functional containing the long-range vdW interactions was also applied.<sup>[56,57]</sup> To optimize the lattice constant of the unit cell, the force on each atom of 0.01 eV Å<sup>-1</sup> and energy convergence of 10<sup>-4</sup> eV were set as the criteria, companying with the energy cutoff of 500 eV.

## Supporting Information

Supporting Information is available from the Wiley Online Library or from the author.

## Acknowledgements

This work was financially supported by the National Natural Science Foundation of China (grant nos. 52072032, 12090031, 12274467, 61761166009, 11974422, 92163206, and 62171035), the 173-JCJQ program (grant no. 2021-JCJQ-JJ-0159), the Ministry of Science and Technology (MOST) of China (grant no. 2018YFE0202700), and the Beijing Nova Program from Beijing Municipal Science & Technology Commission (grant no. Z211100002121072). Calculations were performed at Beijing Super Cloud Computing Center and the Physics Lab of High-Performance Computing of Renmin University of China.

## Conflict of Interest

The authors declare no conflict of interest.

## Author Contributions

J.Z., W.Z., and L.Z. contributed equally to this work. Y.C. and J.Z. conceived this research project and designed the experiment. W.J., J.Q., and W.Z. carried out the DFT calculations (optB86b-vdW functional) and data analysis. L.Z. and F.D. carried out DFT calculations using DFT-D3 and PBE functionals. J.Z. and G.D. performed the Raman measurement and AFM characterizations. J.Z., F.Y. X.W., Y.W., and Q.X. prepared all the samples. Y.C. and J.Z. wrote the manuscript with the necessary input of all authors. All authors have given approval to the final manuscript.

## Data Availability Statement

The data that support the findings of this study are available on request from the corresponding author. The data are not publicly available due to privacy or ethical restrictions.

## Keywords

black arsenic, negative Poisson's ratio, puckered structures, Raman spectroscopy, strain engineering, van der Waals interaction

Received: May 20, 2023

Revised: August 8, 2023

Published online: September 13, 2023

- [1] G. N. Greaves, A. L. Greer, R. S. Lakes, T. Rouxel, *Nat. Mater.* **2011**, *10*, 823.
- [2] L. Augustus, *A Treatise on the Mathematical Theory of Elasticity*, Cambridge University Press, UK **2013**.
- [3] Y. C. Fung, P. Tong, X. Chen, *Classical and Computational Solid Mechanics*, World Scientific Publishing Company, Singapore **2017**.
- [4] E. A. Friis, R. S. Lakes, J. B. Park, *J. Mater. Sci.* **1988**, *23*, 4406.
- [5] J. B. Choi, R. S. Lakes, *Int. J. Fract.* **1996**, *80*, 73.
- [6] R. S. Lakes, *J. Mater. Sci.* **1991**, *26*, 2287.
- [7] S.-I. Park, J. H. Ahn, X. Feng, S. Wang, Y. Huang, J. A. Rogers, *Adv. Funct. Mater.* **2008**, *18*, 2673.
- [8] F. Scarpa, *IEEE Signal Process Mag.* **2008**, *25*, 128.
- [9] R. Lakes, *Science* **1987**, *235*, 1038.
- [10] G. W. Milton, *J. Mech. Phys. Solids* **1992**, *40*, 1105.
- [11] A. Yeganeh-Haeri, D. J. Weidner, J. B. Parise, *Science* **1992**, *257*, 650.
- [12] L. J. Hall, V. R. Coluci, D. S. Galvão, M. E. Kozlov, M. Zhang, S. O. Dantas, R. H. Baughman, *Science* **2008**, *320*, 504.
- [13] Q. H. Wang, K. Kalantar-Zadeh, A. Kis, J. N. Coleman, M. S. Strano, *Nat. Nanotechnol.* **2012**, *7*, 699.
- [14] D. Akinwande, C. Huyghebaert, C.-H. Wang, M. I. Serna, S. Goossens, L.-J. Li, H.-S. P. Wong, F. H. J. Koppens, *Nature* **2019**, *573*, 507.
- [15] A. Yoffe, *Adv. Phys.* **2002**, *51*, 799.
- [16] A. K. Geim, I. V. Grigorieva, *Nature* **2013**, *499*, 419.
- [17] Y. Liu, N. O. Weiss, X. Duan, H.-C. Cheng, Y. Huang, X. Duan, *Nat. Rev. Mater.* **2016**, *1*, 16042.
- [18] X. Wang, Y. Hu, J. Mo, J. Zhang, Z. Wang, W. Wei, H. Li, Y. Xu, J. Ma, J. Zhao, Z. Jin, Z. Guo, *Angew. Chem. Int. Ed.* **2020**, *59*, 5151.
- [19] Y. Hu, Z.-H. Qi, J. Lu, R. Chen, M. Zou, T. Chen, W. Zhang, Y. Wang, X. Xue, J. Ma, Z. Jin, *Chem. Mater.* **2019**, *31*, 4524.
- [20] Y. Hu, X. Wang, Z. Qi, S. Wan, J. Liang, Q. Jia, D. Hong, Y. Tian, J. Ma, Z. Tie, Z. Jin, *Adv. Funct. Mater.* **2021**, *31*, 2106529.
- [21] D. Jariwala, T. J. Marks, M. C. Hersam, *Nat. Mater.* **2017**, *16*, 170.
- [22] N. R. Glavin, R. Rao, V. Varshney, E. Bianco, A. Apte, A. Roy, E. Ringe, P. M. Ajayan, *Adv. Mater.* **2020**, *32*, 1904302.

- [23] Y. Liu, Y. Huang, X. Duan, *Nature* **2019**, *567*, 323.
- [24] H. Qin, Y. Sun, J. Z. Liu, M. Li, Y. Liu, *Nanoscale* **2017**, *9*, 4135.
- [25] J. Wan, J. W. Jiang, H. S. Park, *Nanoscale* **2017**, *9*, 4007.
- [26] Y. Du, J. Maassen, W. Wu, Z. Luo, X. Xu, P. D. Ye, *Nano Lett.* **2016**, *16*, 6701.
- [27] R. Fei, L. Yang, *Appl. Phys. Lett.* **2014**, *105*, 083120.
- [28] Y. Gao, M. Wen, X. Zhang, F. Wu, Q. Xia, H. Wu, H. Dong, *Phys. Chem. Chem. Phys.* **2021**, *23*, 3441.
- [29] J. Han, J. Xie, Z. Zhang, D. Yang, M. Si, D. Xue, *Appl. Phys. Express* **2015**, *8*, 041801.
- [30] J.-W. Jiang, H. S. Park, *Nat. Commun.* **2014**, *5*, 4727.
- [31] L. Yu, Q. Yan, A. Ruzsinszky, *Nat. Commun.* **2017**, *8*, 15224.
- [32] B. Liu, M. Niu, J. Fu, Z. Xi, M. Lei, R. Quhe, *Phys. Rev. Mater.* **2019**, *3*, 054002.
- [33] Y. Hu, J. Liang, Y. Xia, C. Zhao, M. Jiang, J. Ma, Z. Tie, Z. Jin, *Small* **2022**, *18*, 2104556.
- [34] J. Liang, Y. Hu, K. Zhang, Y. Wang, X. Song, A. Tao, Y. Liu, Z. Jin, *Nano Res.* **2022**, *15*, 3737.
- [35] C. Kamal, M. Ezawa, *Phys. Rev. B* **2015**, *91*, 085423.
- [36] Y. Chen, C. Chen, R. Kealhofer, H. Liu, Z. Yuan, L. Jiang, J. Suh, J. Park, C. Ko, H. S. Choe, J. Avila, M. Zhong, Z. Wei, J. Li, S. Li, H. Gao, Y. Liu, J. Analytis, Q. Xia, M. C. Asensio, J. Wu, *Adv. Mater.* **2018**, *30*, 1800754.
- [37] Z. Zhang, J. Xie, D. Yang, Y. Wang, M. Si, D. Xue, *Appl. Phys. Express* **2015**, *8*, 055201.
- [38] M. Zhong, Q. Xia, L. Pan, Y. Liu, Y. Chen, H.-X. Deng, J. Li, Z. Wei, *Adv. Funct. Mater.* **2018**, *28*, 1802581.
- [39] F. Sheng, C. Hua, M. Cheng, J. Hu, X. Sun, Q. Tao, H. Lu, Y. Lu, M. Zhong, K. Watanabe, T. Taniguchi, Q. Xia, Z. A. Xu, Y. Zheng, *Nature* **2021**, *593*, 56.
- [40] L. Kou, Y. Ma, X. Tan, T. Frauenheim, A. Du, S. Smith, *J. Phys. Chem. C* **2015**, *119*, 6918.
- [41] C. Wang, Q. Xia, Y. Nie, M. Rahman, G. Guo, *AIP Adv.* **2016**, *6*, 035204.
- [42] C. Lee, X. Wei, J. W. Kysar, J. Hone, *Science* **2008**, *321*, 385.
- [43] Y. Sun, K. Liu, *J. Appl. Phys.* **2019**, *125*, 082402.
- [44] D. Akinwande, C. J. Brennan, J. S. Bunch, P. Egberts, J. R. Felts, H. Gao, R. Huang, J.-S. Kim, T. Li, Y. Li, K. M. Liechti, N. Lu, H. S. Park, E. J. Reed, P. Wang, B. I. Yakobson, T. Zhang, Y. W. Zhang, Y. Zhou, Y. Zhu, *Extreme Mech. Lett.* **2017**, *13*, 42.
- [45] J. N. Grima, S. Winczewski, L. Mizzi, M. C. Grech, R. Cauchi, R. Gatt, D. Attard, K. W. Wojciechowski, J. Rybicki, *Adv. Mater.* **2015**, *27*, 1455.
- [46] J. Wu, N. Mao, L. Xie, H. Xu, J. Zhang, *Angew. Chem. Int. Ed.* **2015**, *54*, 2366.
- [47] S. B. Desai, G. Seol, J. S. Kang, H. Fang, C. Battaglia, R. Kapadia, J. W. Ager, J. Guo, A. Javey, *Nano Lett.* **2014**, *14*, 4592.
- [48] Y. Li, Z. Hu, S. Lin, S. K. Lai, W. Ji, S. P. Lau, *Adv. Funct. Mater.* **2017**, *27*, 1600986.
- [49] H. J. Conley, B. Wang, J. I. Ziegler, R. F. Haglund Jr, S. T. Pantelides, K. I. Bolotin, *Nano Lett.* **2013**, *13*, 3626.
- [50] R. Zhang, R. Cheung, *Two-Dimensional Materials-Synthesis, Characterization Potential Applications*, InTech, Rijeka, Croatia **2016**, pp. 219–246.
- [51] J. Kim, J.-U. Lee, J. Lee, H. J. Park, Z. Lee, C. Lee, H. Cheong, *Nanoscale* **2015**, *7*, 18708.
- [52] Y. Wang, F. Chen, X. Guo, J. Liu, J. Jiang, X. Zheng, Z. Wang, M. M. Al-Makeen, F. Ouyang, Q. Xia, H. Huang, *J. Phys. Chem. Lett.* **2021**, *12*, 10753.
- [53] M. Dion, H. Rydberg, E. Schröder, D. C. Langreth, B. I. Lundqvist, *Phys. Rev. Lett.* **2004**, *92*, 246401.
- [54] K. Lee, É. D. Murray, L. Kong, B. I. Lundqvist, D. C. Langreth, *Phys. Rev. B* **2010**, *82*, 081101.
- [55] J. P. Perdew, K. Burke, M. Ernzerhof, *Phys. Rev. Lett.* **1996**, *77*, 3865.
- [56] S. Grimme, J. Antony, S. Ehrlich, H. Krieg, *J. Chem. Phys.* **2010**, *132*, 154104.
- [57] S. Grimme, S. Ehrlich, L. Goerigk, *J. Comput. Chem.* **2011**, *32*, 1456.
- [58] L. Li, J. Kim, C. Jin, G. J. Ye, D. Y. Qiu, F. H. Da Jornada, Z. Shi, L. Chen, Z. Zhang, F. Yang, K. Watanabe, T. Taniguchi, W. Ren, S. G. Louie, X. H. Chen, Y. Zhang, F. Wang, *Nat. Nanotechnol.* **2017**, *12*, 21.
- [59] P. E. Blöchl, *Phys. Rev. B* **1994**, *50*, 17953.
- [60] G. Kresse, J. Furthmüller, *Phys. Rev. B* **1996**, *54*, 11169.
- [61] G. Kresse, D. Joubert, *Phys. Rev. B* **1999**, *59*, 1758.
- [62] S. Baroni, S. de Gironcoli, A. Dal Corso, P. Giannozzi, *Rev. Mod. Phys.* **2001**, *73*, 515.
- [63] J. Klimeš, D. R. Bowler, A. Michaelides, *J. Phys.: Condens. Matter* **2009**, *22*, 022201.
- [64] J.-B. Wu, Z. X. Hu, X. Zhang, W. P. Han, Y. Lu, W. Shi, X. F. Qiao, *ACS Nano* **2015**, *9*, 7440.